ISSN (Print) 1226-1750
ISSN (Online) 2233-6656
Journal of Magnetics 31(2), 214-225 (2026) https://doi.org/10.4283/JMAG.2026.31.2.214

Monte Carlo Simulation of Magnetic Shielding for Cs-137 Beta Particles in Radiation Protection

Jeong-Min Seo[1]* and Do-Hun Chin[2]*

[1]*Dept. of Radiological Science, Catholic University of Pusan, #57 Orynndaero, Geumjeonggu, Busan 46252, Republic of Korea*
[2]*Dept. of Industrial Safety & Health, Catholic University of Pusan, #57 Orynndaero, Geumjeonggu, Busan 46252, Republic of Korea*

(Received 28 April 2026, Received in final form 1 June 2026, Accepted 8 June 2026)

This study investigated magnetic deflection shielding for the beta-particle/electron component emitted from Cs-137 using PHITS Monte Carlo simulations. A 1 Ci Cs-137 planar source was modeled in air, and deposited dose rates were evaluated for effective magnetic-field lengths of 1.0, 2.0, and 3.0 cm over magnetic flux densities of 0.0–1.3 T. Photon transport was included in the coupled electron–photon calculation, but deposited dose scoring was restricted to the beta-particle/electron component. At the 30 cm source-to-scoring distance, the 1.0-cm condition showed a minimum dose rate at 0.8 T, followed by dose rebound at higher magnetic flux densities. A similar non-monotonic trend was observed in the additional 15 cm simulation. In contrast, the 2.0- and 3.0-cm conditions reached practical saturation at approximately 0.4 and 0.3 T, respectively. These results demonstrate that compact magnetic deflection shielding should be optimized using the field–length combination rather than magnetic flux density alone, and that effective lengths of 2–3 cm provide a more stable design range for mobile charged-particle shielding devices.

Keywords : radiation, beta particle, shielding, Monte Carlo, Cs-137

1. Introduction

Active magnetic shielding has been investigated as a radiation-protection strategy in which charged particles are deflected by magnetic fields rather than being attenuated solely through passive material absorption. In particular, magnetic shielding has been widely discussed in space radiation protection, where strong magnetic fields are used to reduce exposure to charged cosmic-ray particles. In such systems, the degree of charged-particle deflection is governed not only by magnetic flux density but also by the magnetic field integral, or field–length product, in relation to particle magnetic rigidity [1, 2].

Detailed Monte Carlo studies have also shown that the practical performance of active magnetic shielding should be evaluated by considering the combined effects of magnetic fields, geometry, and surrounding structures [3]. In addition, magnetic-field-induced electron transport has been reported in medical radiation applications, where secondary electrons are deflected by the Lorentz force and consequently modify dose deposition [4]. These studies provide the physical basis for applying magnetic-field-based charged-particle control to radiation-safety applications.

From the perspective of radiation protection, beta particles have often been treated as radiation that can be controlled by relatively simple shielding because their penetration depth is lower than that of photon radiation. However, more sophisticated control strategies may be required in situations involving bremsstrahlung production, exposure to airborne radioactive materials, and protection of radiation-sensitive electronic devices.

Conventional passive shielding methods attenuate beta particles through direct interactions with absorber materials, and such interactions can generate bremsstrahlung photons [5, 6]. In contrast, magnetic deflection shielding can redirect charged beta particles without requiring direct interception by a solid absorber. Therefore, this approach may have the potential to reduce absorber-induced bremsstrahlung as a secondary advantage, although photon fluence and photon dose calculations are required to verify this effect quantitatively.

*Corresponding author:
Tel: +82-51-510-0581, Fax: +82-51-510-0588,
e-mail: thomasjm@naver.com(Jeong-Min Seo)
Tel: +82-51-510-0661, Fax: +82-51-510-0638
e-mail: chindh@cup.ac.kr(Do-Hun Chin)

In the event of an accident at a nuclear facility, some radionuclides released into the atmosphere may remain airborne as aerosol particles for several days to several weeks and may disperse over a wide area depending on meteorological conditions [7]. Among these radionuclides, Cs-137 has a relatively long half-life of approximately 30.17 years and may exist in chemical forms such as water-soluble cesium chloride. Therefore, it can exhibit high environmental mobility and resuspension potential [8]. In assessments of the Chernobyl and Fukushima accidents, Cs-137 has been identified as a major contributor to both external and internal exposure [9]. Cs-137 emits beta particles through two principal decay branches: a dominant branch with an endpoint energy of approximately 514 keV and a minor branch with an endpoint energy of approximately 1.176 MeV. These beta particles may contribute to the absorbed dose in superficial tissues, particularly the skin, and therefore should be considered in external beta-radiation protection assessments [10, 11]. Accordingly, Cs-137 is an important radionuclide for which beta-particle shielding should be carefully considered [5, 6].

A previous simulation study evaluated magnetic deflection shielding for the beta-particle/electron component emitted from Cs-137 using effective magnetic-field lengths of 5 and 10 cm [12]. In that study, a 1 Ci Cs-137 planar source was modeled in air, and a 40 × 40 × 5 cm^3 dose-scoring volume was placed 30 cm from the source.

Although photon transport was included in the simulation, the deposited dose scored in the dose-scoring volume was restricted to the beta-particle/electron component. Therefore, the reported dose values represented the absorbed dose from Cs-137 beta particles rather than the total absorbed dose from all radiation components emitted by Cs-137.

Furthermore, the previous simulation study showed that effective magnetic-field lengths of 5 and 10 cm produced dose reductions greater than approximately 88% even at a relatively low magnetic flux density of 0.2 T. This indicates that the 5–10 cm field lengths were already sufficiently long for the Cs-137 beta-particle spectrum and that the dose-reduction response was close to saturation under those conditions. These findings provided the basis for the present work but did not resolve the compact finite-length regime relevant to miniaturized shielding structures. Therefore, the present study focuses on shorter effective magnetic-field lengths of 1–3 cm to investigate the finite-length transport regime that could not be resolved under the previous 5–10 cm conditions. Under such compact-field conditions, shielding performance is expected to depend on the combined effect of magnetic flux density and effective magnetic-field length, rather than on magnetic flux density alone. This shortened field-length range was selected to identify the transition among insufficient beta-particle deflection, practical dose-reduction saturation, and trajectory over-deflection.

The present study was designed as a preliminary simulation study for the development of compact and mobile active shielding devices for charged particles emitted from beta-emitting radionuclides such as Cs-137. In practical radiation-safety operations, radiation fields containing airborne or deposited beta-emitting radioactive materials may be encountered by workers as well as by mobile equipment, including radiation-measuring instruments, inspection robots, and drones. Mobile radiation detection systems and unmanned aerial platforms have been increasingly investigated for radiation mapping, source localization, and emergency monitoring in contaminated or post-accident environments [13, 14]. Although these systems can reduce direct human access to hazardous areas, their onboard detectors, electronic components, and control systems may still operate within radiation fields. Therefore, localized charged-particle shielding may be useful for protecting workers and radiation-sensitive mobile equipment in beta-emitting radioactive environments.

For these applications, the shielding structure must be compact, lightweight, and installable within a limited space. Consequently, the effective magnetic-field length cannot be increased arbitrarily, even if a longer magnetic-field region provides a higher probability of particle deflection. This practical constraint provides an engineering rationale for evaluating effective magnetic-field lengths of 1–3 cm. Thus, the shortened field-length regime evaluated in this study is directly relevant to compact mobile magnetic shielding structures and provides new insight into field–length-dependent beta-particle transport and the operating window required for mobile magnetic deflection shielding.

2. Materials and Methods

2.1. Monte Carlo Simulation Code and Source Definition

Radiation transport was simulated using PHITS, the Particle and Heavy Ion Transport code System, version 3.350, a general-purpose Monte Carlo radiation transport code [15]. PHITS was developed mainly by the Japan Atomic Energy Agency (JAEA) and can transport various radiation particles, including neutrons, protons, heavy ions, photons, electrons, and positrons, over a wide energy range. In addition, PHITS can model magnetic fields, such as dipole and quadrupole fields, and can therefore be used to evaluate the magnetic deflection of charged particles [16].

The radionuclide considered in this study was Cs-137, which primarily undergoes beta-minus decay to Ba-137m, followed by the emission of a 661.7 keV gamma ray during the transition of Ba-137m to the ground state. The beta-particle energy distribution of Cs-137 depends on the decay branch. In the dominant branch to Ba-137m, with a branching ratio of approximately 94.4%, beta particles have a maximum energy of approximately 514.0 keV and a mean energy of approximately 173.7 keV. In the direct decay branch to Ba-137, with a branching ratio of approximately 5.6%, beta particles have a maximum energy of approximately 1,175.6 keV and a mean energy of approximately 416.3 keV [17].

The Cs-137 source was modeled using the built-in radioisotope source option in PHITS. The source activity was set to 3.7×10^{10} Bq, corresponding to 1 Ci. The radioisotope source option generated the electron emission spectrum from radioactive decay data; therefore, the source was not approximated by a monoenergetic or mean-energy beta source. Instead, the continuous beta-particle spectrum and decay-related electron emissions, including Auger and internal conversion electrons, were included in the source sampling.

Electron and photon transport was handled using the EGS5-based electron–photon transport mode implemented in PHITS. Therefore, bremsstrahlung photons generated during electron transport were included in the particle transport calculation. However, the deposited dose reported in this study was restricted to the beta-particle/electron component in the dose-scoring volume. Photon dose and total absorbed dose from all radiation components emitted by Cs-137 were not used as outcome quantities. Accordingly, the reported deposited dose values should be interpreted as the absorbed dose from the beta-particle/electron component of Cs-137, rather than as the total absorbed dose from all Cs-137 radiation components.

2.2. Simulation Geometry and Source-to-Scoring Distance

The simulation space was defined as air under International Standard Atmosphere conditions. The CSDA range of Cs-137 beta particles in dry air was set to approximately 0.04103 g/cm^2 [18]. By applying the air density used in the simulation, the representative mean range of Cs-137 beta particles in air was estimated to be approximately 33.5 cm. Considering both the mean beta-particle range and the possible maximum range exceeding approximately 1 m for the high-energy beta component, the primary source-to-scoring distance was set to 30 cm. This distance was selected as a representative benchmark at which a substantial fraction of Cs-137 beta particles can still reach the dose-scoring volume, while energy loss and range-out in air remain relevant.

To evaluate the dependence of magnetic shielding performance on the source-to-scoring distance, an additional sensitivity simulation was performed at a shorter distance of 15 cm. This distance was selected as a representative shorter standoff condition corresponding to half of the primary 30 cm geometry. In the 15 cm simulation, all other parameters, including source size, source activity, magnetic-field geometry, effective magnetic-field length, dose-scoring volume, number of histories, and tally conditions, were kept identical to those used in the 30 cm simulation, except that the source plane was moved closer to the source-side boundary of the dose-scoring volume.

The beta-emitting source was modeled as a square planar surface source with dimensions of 100 cm × 100 cm. Beta particles were emitted unidirectionally toward the magnetic-field region and the dose-scoring volume. This source geometry was selected as a conservative representation of exposure to a broad beta-emitting radioactive field, such as an airborne or deposited Cs-137

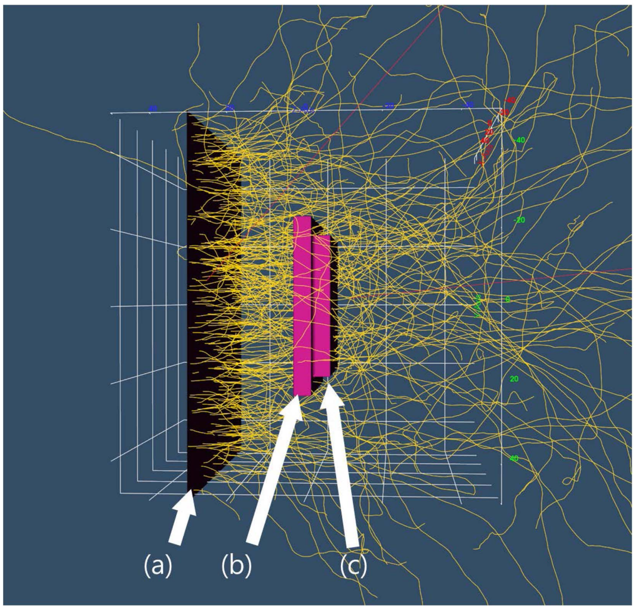

Fig. 1. (Color online) Geometrical configuration of the PHITS simulation model for the source-to-scoring distance of 30 cm. The model consists of (a) a Cs-137 planar surface source emitting beta particles unidirectionally, (b) the magnetic-field region, and (c) the deposited dose evaluation region. The yellow lines represent the simulated trajectories of beta particles, whereas the red line represents a photon trajectory. This geometry was used to evaluate the magnetic deflection behavior of the beta-particle/electron component emitted from Cs-137 at a source-to-scoring distance of 30 cm.

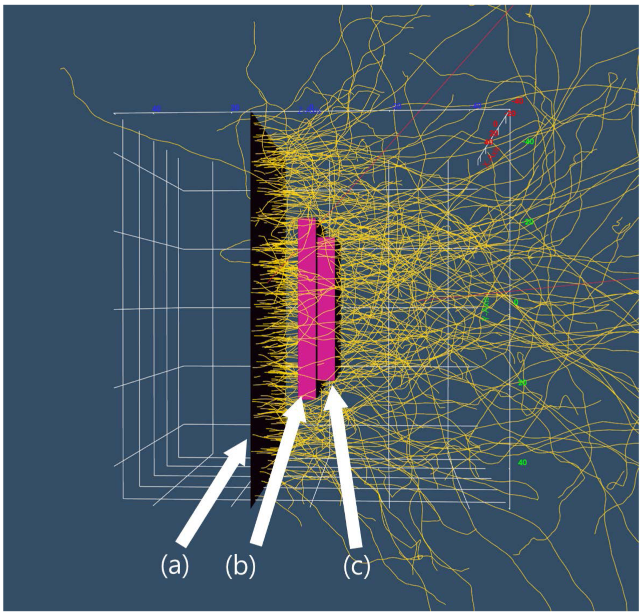

Fig. 2. (Color online) Geometrical configuration of the PHITS simulation model for the source-to-scoring distance of 15 cm. The model consists of (a) a Cs-137 planar surface source emitting beta particles unidirectionally, (b) the magnetic-field region, and (c) the deposited dose evaluation region. The yellow lines represent the simulated trajectories of beta particles, whereas the red line represents a photon trajectory. This geometry was used to evaluate the magnetic deflection behavior of the beta-particle/electron component emitted from Cs-137 at a source-to-scoring distance of 15 cm.

contamination environment. The geometrical configurations of the PHITS simulation models for the source-to-scoring distances of 30 and 15 cm are shown in Figs. 1 and 2, respectively.

2.3. Magnetic Field Configuration

The magnetic field was modeled as an idealized uniform dipole field to isolate the effects of magnetic flux density and effective magnetic-field length on the transport of Cs-137 beta particles. The magnetic field was arranged perpendicular to the beta-particle transport. The pole gap and pole width were each set to 50 cm in consideration of the beta-particle fluence and the transverse size of the irradiation geometry.

The magnetic-field region was positioned immediately upstream of the dose-scoring volume, extending from the source-side boundary of the dose-scoring volume toward the source. The effective magnetic-field length was defined as the distance over which beta particles passed through the magnetic-field region. To evaluate the finite-length effect relevant to compact and mobile magnetic shielding structures, effective magnetic-field lengths of 1.0, 2.0, and 3.0 cm were examined. For each effective magnetic-field length, magnetic flux densities from 0.0 to 1.3 T were evaluated at intervals of 0.1 T.

It should be noted that the magnetic-field model used in this study was an idealized uniform-field approximation. Fringe fields and spatial non-uniformity near practical magnet edges were not included in the present model. Therefore, the results should be interpreted as a physical benchmark for compact magnetic deflection shielding rather than as a final engineering model of a specific magnet assembly.

2.4. Dose-Scoring Volume and Tally Conditions

The purpose of the dose evaluation was not to estimate organ or tissue absorbed dose in the human body, but to assess the feasibility of magnetic-field-based active shielding for charged particles. Accordingly, the dose-scoring volume was defined as an air volume immediately downstream of the magnetic-field region. The transverse area was set to 40 cm × 40 cm, and the depth was set to 5.0 cm along the beta-particle transport direction. Thus, the geometrical size of the dose-scoring volume was 40 cm × 40 cm × 5 cm.

Absorbed dose was evaluated using the PHITS [T-Deposit] tally with a region-wise mesh in the dose-scoring volume. The dose scoring was restricted to the electron component in order to evaluate the deposited dose from the beta-particle/electron component of Cs-137. The tally output was obtained as absorbed dose per source particle (Gy/source) and was normalized to a unit air volume of 1 cm^3. The corresponding absorbed dose rate (Gy/s) was calculated for the 1 Ci Cs-137 source by applying the source activity of 3.7×10^{10} s^{-1}.

Electron fluence maps were additionally obtained using the PHITS [T-Track] tally on an xy-mesh at the entrance side of the dose-scoring volume. These fluence maps were used to visualize the spatial distribution of beta particles entering the dose-scoring volume under different magnetic-field conditions.

2.5. Transport Parameters and Statistical Uncertainty

For each simulation condition, a total of 2.0×10^6 source histories were simulated, consisting of 500,000 histories per batch and four batches. Electron and bremsstrahlung photon transport was performed using the EGS5-based electron–photon transport mode implemented in PHITS (negs=1) [19]. No user-defined cut-off energies were specified in the input file; therefore, the default PHITS/EGS5 cut-off settings were applied, corresponding to 0.1 MeV for electrons and positrons and 0.001 MeV for photons.

Statistical uncertainty was evaluated using the history-variance method reported by PHITS. The relative error (r.err) of each deposited dose value was obtained from the PHITS [T-Deposit] output. The absolute statistical uncertainty was calculated by multiplying the deposited dose rate by the corresponding relative error. These uncertainty values were included in the tables and were used as error bars in the dose-rate figures. The relative errors of the deposited dose values were less than 2.6% for all simulation conditions, indicating adequate statistical convergence. Because the statistical uncertainties were relatively small, some error bars are smaller than or comparable to the plotted symbols.

3. Results

Table 1 summarizes the deposited dose rates and statistical uncertainties for the source-to-scoring distance of 30 cm, and Table 2 summarizes the corresponding results for the shorter distance of 15 cm. The statistical uncertainties were calculated from the relative errors reported by PHITS and are shown as error bars in the dose-rate figures. Because the relative errors were small for all simulation conditions, several error bars are smaller than or comparable to the plotted symbols.

Figs. 3 and 4 show the deposited dose-rate curves with statistical error bars for the 30 and 15 cm source-to-scoring distances, respectively. The error bars were calculated as the product of the deposited dose rate and the PHITS-reported relative error. In both figures, the error bars are small relative to the scale of the dose-rate variation, reflecting the statistical convergence of the simulations. The graphical trends are consistent with the quantitative values listed in Tables 1 and 2.

3.1. Deposited Dose Rate at a Source-to-Scoring Distance of 30 cm

At the source-to-scoring distance of 30 cm, the deposited dose rates under the no-magnetic-field condition were 8.8799, 8.8805, and 8.8822 Gy/s, respectively. These values were essentially identical, indicating that the baseline dose rate was independent of the assigned magnetic-field length when no magnetic field was applied.

When the magnetic field was applied, the dose-rate reduction strongly depended on the effective magnetic-field length. For the 1.0-cm condition, the dose rate decreased gradually from 8.8799 Gy/s at 0.0 T to 7.4095 Gy/s at 0.1 T, 2.6066 Gy/s at 0.4 T, and 1.4962 Gy/s at 0.6 T. The minimum dose rate was 1.3028 Gy/s at 0.8 T, corresponding to an 85.33% reduction relative to the no-field condition. However, above 0.8 T, the dose rate increased again, reaching 1.3801, 1.4231, 1.4532, and

Table 1. Deposited dose rates of Cs-137 beta particles at a source-to-scoring distance of 30 cm according to magnetic flux density and effective magnetic-field length.

Magnetic flux density, B (T)	Deposited dose rate ± statistical uncertainty (Gy/s)		
	1 cm	2 cm	3 cm
0.0	8.8799 ± 0.0586 (0.66%)	8.8805 ± 0.0586 (0.66%)	8.8822 ± 0.0586 (0.66%)
0.1	7.4095 ± 0.0526 (0.71%)	5.2176 ± 0.0438 (0.84%)	3.1041 ± 0.0341 (1.10%)
0.2	5.4488 ± 0.0447 (0.82%)	2.0352 ± 0.0295 (1.45%)	1.0763 ± 0.0252 (2.34%)
0.3	3.6637 ± 0.0366 (1.00%)	1.0859 ± 0.0249 (2.29%)	0.9791 ± 0.0242 (2.47%)
0.4	2.6066 ± 0.0321 (1.23%)	0.9879 ± 0.0242 (2.45%)	0.9525 ± 0.0239 (2.51%)
0.5	1.9429 ± 0.0293 (1.51%)	0.9718 ± 0.0242 (2.49%)	0.9533 ± 0.0240 (2.52%)
0.6	1.4962 ± 0.0272 (1.82%)	0.9749 ± 0.0244 (2.50%)	0.9569 ± 0.0242 (2.53%)
0.7	1.3168 ± 0.0265 (2.01%)	0.9499 ± 0.0239 (2.52%)	0.9381 ± 0.0238 (2.54%)
0.8	1.3028 ± 0.0264 (2.03%)	0.9442 ± 0.0239 (2.53%)	0.9334 ± 0.0238 (2.55%)
0.9	1.3059 ± 0.0261 (2.00%)	0.9492 ± 0.0238 (2.51%)	0.9287 ± 0.0237 (2.55%)
1.0	1.3801 ± 0.0268 (1.94%)	0.9569 ± 0.0239 (2.50%)	0.9369 ± 0.0238 (2.54%)
1.1	1.4231 ± 0.0272 (1.91%)	0.9571 ± 0.0240 (2.51%)	0.9345 ± 0.0238 (2.55%)
1.2	1.4532 ± 0.0273 (1.88%)	0.9708 ± 0.0240 (2.47%)	0.9298 ± 0.0236 (2.54%)
1.3	1.4972 ± 0.0277 (1.85%)	0.9712 ± 0.0240 (2.47%)	0.9326 ± 0.0237 (2.54%)

Note.
Values are presented as deposited dose rate ± statistical uncertainty (relative error, %). The statistical uncertainty was calculated by multiplying the deposited dose rate by the relative error reported by PHITS. The deposited dose rate was normalized to 1 cm^3 of air and calculated for a 1 Ci Cs-137 source at a source-to-scoring distance of 30 cm. Photon transport was included in the coupled electron–photon transport calculation; however, deposited dose scoring was restricted to the beta-particle/electron component.

Table 2. Deposited dose rates of Cs-137 beta particles at a source-to-scoring distance of 15 cm according to magnetic flux density and effective magnetic-field length.

Magnetic flux density, B (T)	Deposited dose rate ± statistical uncertainty (Gy/s)		
	1 cm	2 cm	3 cm
0.0	13.5120 ± 0.0730 (0.54%)	13.5110 ± 0.0730 (0.54%)	13.5120 ± 0.0730 (0.54%)
0.1	11.7640 ± 0.0671 (0.57%)	8.0216 ± 0.0553 (0.69%)	4.5089 ± 0.0424 (0.94%)
0.2	8.4998 ± 0.0569 (0.67%)	2.8523 ± 0.0368 (1.29%)	1.6632 ± 0.0318 (1.91%)
0.3	5.3722 ± 0.0451 (0.84%)	1.6755 ± 0.0320 (1.91%)	1.5985 ± 0.0315 (1.97%)
0.4	3.7526 ± 0.0398 (1.06%)	1.5965 ± 0.0315 (1.97%)	1.5808 ± 0.0313 (1.98%)
0.5	2.6767 ± 0.0364 (1.36%)	1.5795 ± 0.0314 (1.99%)	1.5688 ± 0.0312 (1.99%)
0.6	2.0715 ± 0.0338 (1.63%)	1.5607 ± 0.0311 (1.99%)	1.5503 ± 0.0310 (2.00%)
0.7	1.8846 ± 0.0330 (1.75%)	1.5627 ± 0.0311 (1.99%)	1.5452 ± 0.0309 (2.00%)
0.8	1.8961 ± 0.0332 (1.75%)	1.5575 ± 0.0310 (1.99%)	1.5432 ± 0.0309 (2.00%)
0.9	1.9237 ± 0.0333 (1.73%)	1.5488 ± 0.0310 (2.00%)	1.5378 ± 0.0309 (2.01%)
1.0	1.9720 ± 0.0335 (1.70%)	1.5566 ± 0.0311 (2.00%)	1.5345 ± 0.0310 (2.02%)
1.1	2.0251 ± 0.0336 (1.66%)	1.5591 ± 0.0310 (1.99%)	1.5345 ± 0.0308 (2.01%)
1.2	2.0949 ± 0.0341 (1.63%)	1.5620 ± 0.0309 (1.98%)	1.5324 ± 0.0308 (2.01%)
1.3	2.1781 ± 0.0346 (1.59%)	1.5706 ± 0.0309 (1.97%)	1.5380 ± 0.0308 (2.00%)

Note.
Values are presented as deposited dose rate ± statistical uncertainty (relative error, %). The statistical uncertainty was calculated by multiplying the deposited dose rate by the relative error reported by PHITS. The deposited dose rate was normalized to 1 cm³ of air and calculated for a 1 Ci Cs-137 source at a source-to-scoring distance of 15 cm. Photon transport was included in the coupled electron–photon transport calculation; however, deposited dose scoring was restricted to the beta-particle/electron component.

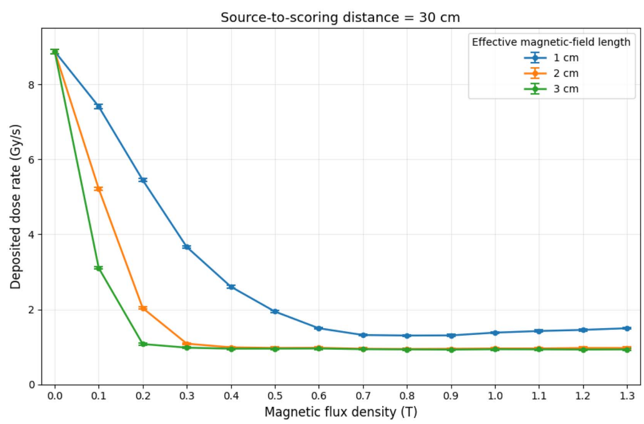

Fig. 3. (Color online) Deposited dose rates of Cs-137 beta particles in the dose-scoring volume as a function of magnetic flux density at a source-to-scoring distance of 30 cm. The effective magnetic-field lengths were 1, 2, and 3 cm. Error bars represent statistical uncertainties calculated from the relative errors reported by PHITS. The 2- and 3-cm conditions showed rapid dose reduction followed by practical saturation, whereas the 1-cm condition exhibited a non-monotonic response, with a dose rebound at higher magnetic flux densities. This rebound suggests trajectory over-deflection under a short effective magnetic-field length.

1.4972 Gy/s at 1.0, 1.1, 1.2, and 1.3 T, respectively. This non-monotonic response indicates that the 1.0-cm effective magnetic-field length has an optimal operating region near 0.8 T, beyond which dose rebound occurs. Exceeding this threshold leads to trajectory over-deflection,

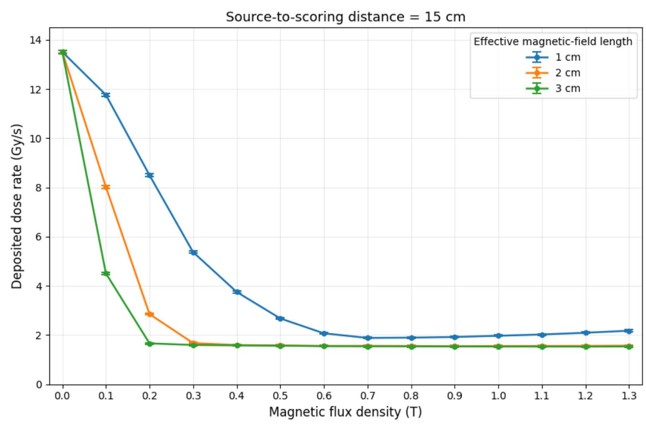

Fig. 4. (Color online) Deposited dose rates of Cs-137 beta particles in the dose-scoring volume as a function of magnetic flux density at a source-to-scoring distance of 15 cm. The effective magnetic-field lengths were 1, 2, and 3 cm. Error bars represent statistical uncertainties calculated from the relative errors reported by PHITS. Similar to the 30 cm condition, the 1-cm effective magnetic-field length showed a non-monotonic dose response, with dose rebound at higher magnetic flux densities. In contrast, the 2- and 3-cm conditions exhibited rapid dose reduction followed by practical saturation, indicating more stable magnetic deflection behavior under the shorter source-to-scoring distance.

inadvertently redirecting beta particles back into the dose-scoring volume.

For the 2.0-cm condition, the dose rate decreased more rapidly than in the 1.0-cm condition. The deposited dose rate was reduced to 5.2176 Gy/s at 0.1 T, 2.0352 Gy/s at 0.2 T, and 1.0859 Gy/s at 0.3 T. At magnetic flux densities of 0.4 T and higher, the dose rate remained within a narrow range of 0.9442–0.9879 Gy/s, indicating practical saturation. The minimum value was 0.9442 Gy/s at 0.8 T, corresponding to an 89.37% reduction relative to the no-field condition. The subsequent increase at higher magnetic flux densities was small; at 1.3 T, the dose rate was 0.9712 Gy/s, only 2.86% higher than the minimum value.

For the 3.0-cm condition, practical saturation was reached at a lower magnetic flux density. The dose rate decreased sharply to 3.1041 Gy/s at 0.1 T and 1.0763 Gy/s at 0.2 T. At 0.3 T, the dose rate was 0.9791 Gy/s, after which it remained within a narrow range of 0.9287–0.9791 Gy/s. The minimum dose rate was 0.9287 Gy/s at 0.9 T, corresponding to an 89.54% reduction relative to the no-field condition. The dose rates at 1.2 and 1.3 T were 0.9298 and 0.9326 Gy/s, respectively, which were nearly identical to the minimum value. These results indicate that the 3.0-cm condition reached practical saturation at approximately 0.3 T.

Overall, at 30 cm, the 3.0-cm effective magnetic-field length showed the fastest approach to saturation, followed by the 2.0-cm condition. The 1.0-cm condition required a higher magnetic flux density to reach its minimum dose rate and exhibited dose rebound in the high-field region.

3.2. Deposited Dose Rate at a Source-to-Scoring Distance of 15 cm

The additional 15 cm simulation was performed to evaluate whether the length-dependent magnetic shielding behavior observed at 30 cm was maintained under a shorter source-to-scoring distance. As expected, the absolute deposited dose rates under the no-magnetic-field condition were higher at 15 cm than at 30 cm because of the shorter air transport distance. The no-field dose rates were 13.5120, 13.5110, and 13.5120 Gy/s, respectively.

For the 1.0-cm condition at 15 cm, the dose rate decreased from 13.5120 Gy/s at 0.0 T to 11.7640 Gy/s at 0.1 T, 8.4998 Gy/s at 0.2 T, 5.3722 Gy/s at 0.3 T, and 2.0715 Gy/s at 0.6 T. The minimum dose rate was 1.8846 Gy/s at 0.7 T, corresponding to an 86.05% reduction relative to the no-field condition. However, similar to the 30 cm result, a dose rebound was observed at higher magnetic flux densities. The dose rate increased to 1.9720, 2.0251, 2.0949, and 2.1781 Gy/s at 1.0, 1.1, 1.2, and 1.3 T, respectively. At 1.3 T, the dose rate was 15.57% higher than the minimum value. This confirms that the non-monotonic response of the 1.0-cm condition was not specific to the 30 cm geometry.

For the 2.0-cm condition at 15 cm, the dose rate decreased rapidly to 8.0216 Gy/s at 0.1 T, 2.8523 Gy/s at 0.2 T, and 1.6755 Gy/s at 0.3 T. At and above 0.4 T, the dose rate remained nearly constant within the range of 1.5488–1.5965 Gy/s. The minimum value was 1.5488 Gy/s at 0.9 T, corresponding to an 88.54% reduction relative to the no-field condition. The dose rate at 1.3 T was 1.5706 Gy/s, only 1.41% higher than the minimum value, indicating a stable saturation response.

For the 3.0-cm condition at 15 cm, the dose rate decreased most rapidly. The dose rate was reduced to 4.5089 Gy/s at 0.1 T and 1.6632 Gy/s at 0.2 T. From 0.3 T onward, the dose rate remained within a narrow range of 1.5324–1.5985 Gy/s. The minimum value was 1.5324 Gy/s at 1.2 T, corresponding to an 88.66% reduction relative to the no-field condition. The dose rate at 1.3 T was 1.5380 Gy/s, which was nearly identical to the minimum value. Thus, the 3.0-cm condition also showed practical saturation under the 15 cm geometry.

3.3. Particle Trajectories and Spatial Flux Distribution due to Magnetic Field

The particle-track visualization further supported the dose-rate results. Fig. 5 shows representative particle trajectories at source-to-scoring distances of 30 and 15 cm under the no-field condition and under a magnetic flux density of 0.2 T with a 1.0-cm effective magnetic-field length. Under the no-field condition, beta-particle tracks propagated toward the dose-scoring region without magnetic deflection. When the magnetic field was applied, the charged-particle trajectories were redistributed by the Lorentz force, indicating that even a short 1.0-cm magnetic-field region can modify beta-particle transport before the particles enter the dose-scoring volume.

Fig. 6 shows the spatial flux distributions of beta particles at the entrance side of the dose-scoring volume for source-to-scoring distances of 30 and 15 cm. For each distance, the no-field condition was compared with 0.5 T magnetic-field conditions using effective magnetic-field lengths of 1.0, 2.0, and 3.0 cm. The no-field maps showed a relatively symmetric flux distribution centered on the transport direction, whereas the magnetic-field cases showed length-dependent redistribution of beta-particle flux. As the effective magnetic-field length increased, the beta-particle flux entering the dose-scoring region became increasingly redistributed, supporting the quantitative finding that longer effective magnetic-field lengths reach practical saturation at lower magnetic flux densities.

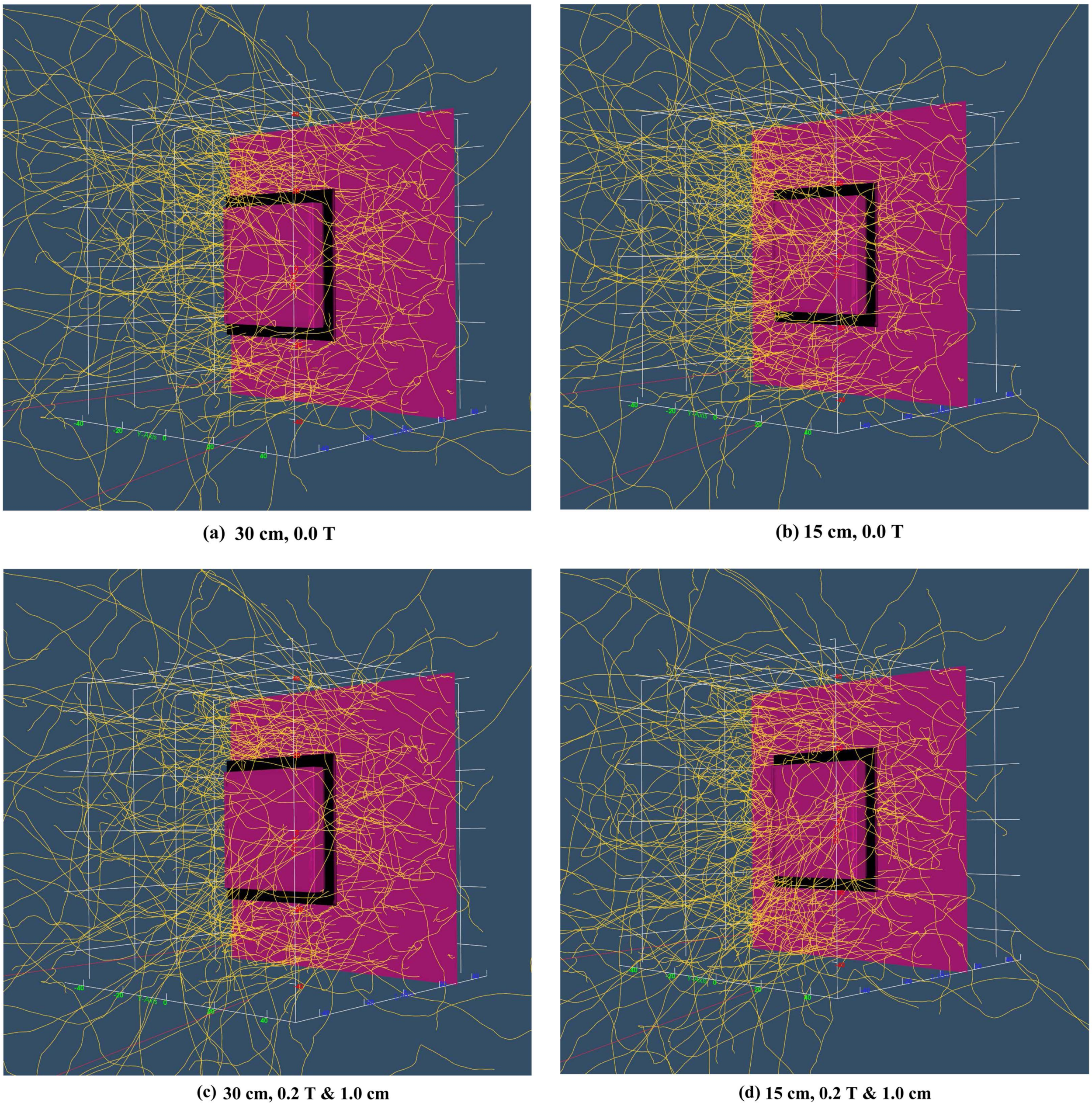

Fig. 5. (Color online) Representative PHITS particle-track 3D visualizations for source-to-scoring distances of 30 and 15 cm. (a) 30 cm, 0.0 T; (b) 15 cm, 0.0 T; (c) 30 cm, 0.2 T with a 1.0-cm effective magnetic-field length; and (d) 15 cm, 0.2 T with a 1.0-cm effective magnetic-field length. Yellow tracks indicate beta-particle/electron trajectories, and red tracks indicate photon trajectories. The comparison illustrates the magnetic-field-induced redistribution of charged-particle transport under the shortened effective magnetic-field condition.

Similar spatial trends were observed at both 30 and 15 cm, although the 15 cm condition retained higher overall particle flux because of the shorter air transport distance.

The 15 cm simulation produced higher absolute deposited dose rates than the 30 cm simulation because beta particles traveled a shorter distance in air before reaching the magnetic-field region and dose-scoring volume. Nevertheless, the overall length-dependent trend was preserved at both distances. In both the 30 and 15 cm geometries, the 3.0-cm condition approached saturation at lower magnetic flux densities, the 2.0-cm condition showed a stable plateau after rapid dose reduction, and the 1.0-cm condition showed a broader transition region followed by dose rebound at higher magnetic flux densities.

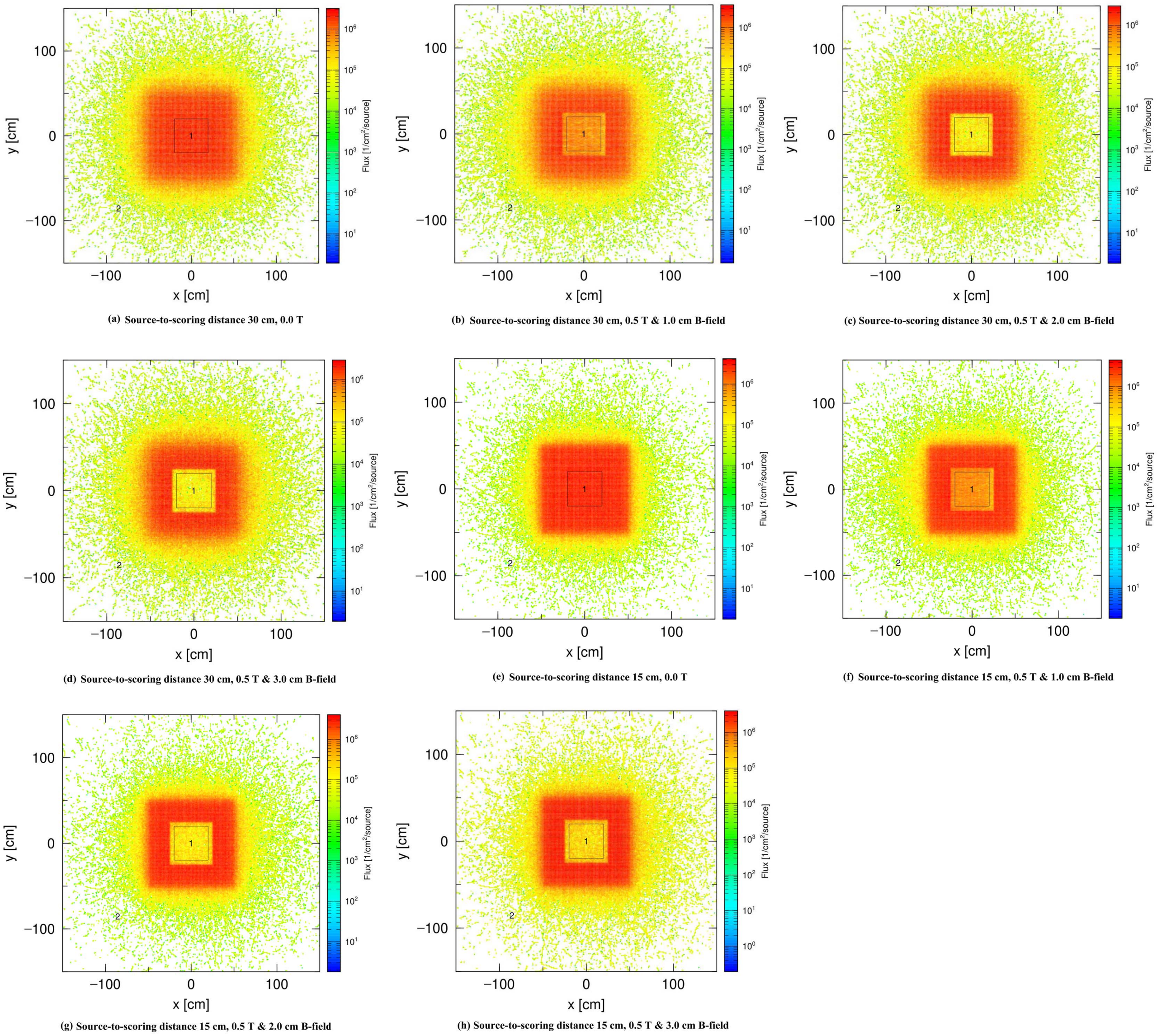

Fig. 6. (Color online) Spatial flux distributions of beta particles at the entrance side of the dose-scoring volume for source-to-scoring distances of 30 and 15 cm. The square marked “1” denotes the entrance surface of the dose-scoring volume. Panels (a)–(d) show the 30 cm condition, and panels (e)–(h) show the 15 cm condition. The no-field conditions are shown in panels (a) and (e), whereas 0.5 T magnetic-field conditions with effective magnetic-field lengths of 1.0, 2.0, and 3.0 cm are shown in panels (b)–(d) and (f)–(h), respectively. The maps show the length-dependent redistribution of beta-particle fluence caused by magnetic deflection.

These results indicate that the finite-length magnetic-field effect observed in this study was not limited to a single source-to-scoring distance. Rather, the shielding behavior was governed by the combined effect of magnetic flux density and effective magnetic-field length. In particular, the repeated observation of dose rebound in the 1.0-cm condition at both 30 and 15 cm supports the interpretation that an excessively short magnetic-field region can produce non-monotonic transport behavior at high magnetic flux densities.

4. Discussion

The present study was designed to clarify the finite-length behavior of magnetic deflection shielding for the beta-particle/electron component emitted from Cs-137. In a previous simulation study, effective magnetic-field lengths of 5 and 10 cm were evaluated using a comparable broad-field geometry [12]. In that study, the dose rate decreased from 8.8815 Gy/s without a magnetic field to 1.00730–0.92433 Gy/s for the 5-cm condition and to

0.99116–0.90366 Gy/s for the 10-cm condition over magnetic flux densities of 0.2–1.0 T. These values corresponded to dose reductions exceeding approximately 88.7%, indicating that the 5–10 cm field lengths were already sufficiently long for the Cs-137 beta-particle spectrum and that the dose-reduction response was close to saturation under those conditions. In contrast, the present study demonstrated that when the effective magnetic-field length was shortened to 1–3 cm, the dose-reduction behavior became strongly dependent on the field–length combination.

Therefore, the present study is not merely a simple parameter extension of the previous study, but rather identifies a compact finite-length regime in which insufficient deflection, practical saturation, and trajectory over-deflection can be distinguished.

The importance of the field–length combination can be understood from the magnetic rigidity of the high-energy tail of the Cs-137 beta spectrum. When the 1.176 MeV endpoint-energy electron is used as a representative high-rigidity component, the magnetic flux densities required to produce an approximately 90° deflection over effective magnetic-field lengths of 1, 2, and 3 cm are estimated to be approximately 0.84, 0.42, and 0.28 T, respectively. These estimates are consistent with the simulation results. The 3-cm condition approached practical saturation at approximately 0.3 T, the 2-cm condition reached a plateau at approximately 0.4 T, and the 1-cm condition showed a transition in dose response around 0.8–0.9 T. These findings suggest that the practical transition point in compact magnetic shielding is governed by the field–length product required to deflect the high-rigidity component of the beta-particle spectrum.

The dose rebound observed in the 1-cm condition should not be interpreted as a violation of the Lorentz force principle or as physically unrealistic behavior caused by an excessively strong magnetic field. Instead, it can be interpreted as a finite-geometry transport effect. In a very short magnetic-field region, increasing the magnetic flux density enhances the curvature of charged-particle trajectories; however, beyond an optimal range, part of the high-energy electron component may be redirected toward the dose-scoring volume. This produces a non-monotonic mapping of charged-particle trajectories into the scoring region, which can be described as trajectory over-deflection or over-bending. Similar magnetic-field-induced dose perturbations have been reported in radiological systems involving transverse magnetic fields. For example, Ahn *et al.* showed that a localized 0.5 T transverse magnetic field can generate both dose-enhancement and dose-reduction regions in an inhomogeneous phantom, indicating that magnetic-field-induced dose modification depends on particle transport geometry, field configuration, and boundary conditions [20]. This supports the interpretation that the rebound observed in the present 1-cm condition is a geometry-dependent charged-particle transport effect.

The additional 15 cm simulation further supports this interpretation. The absolute deposited dose rates were higher at 15 cm than at 30 cm because beta particles traveled a shorter distance in air before reaching the magnetic-field region and the dose-scoring volume. Nevertheless, the overall length-dependent trend was maintained. At both source-to-scoring distances, the 3-cm condition approached saturation at relatively low magnetic flux densities, the 2-cm condition showed a stable plateau after rapid dose reduction, and the 1-cm condition exhibited dose rebound at higher magnetic flux densities. Therefore, the finite-length behavior observed in this study was not specific to the 30 cm geometry. Rather, it reflects the combined effects of magnetic flux density, effective magnetic-field length, source-to-scoring distance, and beta-particle transport in air.

From a practical design perspective, these results indicate that miniaturization of a magnetic deflection shielding device cannot be achieved simply by increasing the magnetic flux density. The 1-cm configuration provided dose reduction up to an optimal magnetic flux density, but it also showed rebound at higher field strengths. Therefore, a 1-cm effective magnetic-field length should be considered only when severe spatial constraints are imposed, and the operating magnetic flux density should be carefully selected to avoid over-deflection. In contrast, the 2–3 cm configurations provided more stable dose-reduction behavior and reached practical saturation at lower magnetic flux densities. For compact mobile shielding systems intended for beta-emitting radioactive fields, such as localized protection of workers, survey meters, robotic inspection platforms, and drones, the 2–3 cm range may therefore provide a more practical design window than the 1-cm configuration.

The present findings are also consistent with previous Monte Carlo-based studies of active shielding, which showed that shielding performance depends on geometry, material configuration, and charged-particle transport rather than on magnetic field strength alone. Vuolo et al. reported that the apparent efficiency of active magnetic shielding can be substantially altered when realistic structures and materials are included in the Monte Carlo model, because secondary radiation generated in surrounding materials can reduce the net shielding benefit [3]. Although the present study did not include a massive supporting structure, the same principle applies to compact beta-particle shielding: magnetic flux density alone is insufficient to characterize shielding performance, and finite field length, source-to-scoring geometry, and charged-particle transport behavior must be considered together.

Several limitations should be noted. First, the present simulation used an idealized uniform dipole magnetic field to isolate the effects of magnetic flux density and effective magnetic-field length. In practical magnet systems, the magnetic field is not perfectly uniform and does not terminate abruptly at the boundary of the nominal field region. Fringe fields near the pole edges may alter the accumulated magnetic deflection, the effective magnetic-field length, and the spatial distribution of beta particles entering the dose-scoring volume. Therefore, the present results should be interpreted as an idealized physical benchmark for compact magnetic deflection shielding rather than as a final engineering design of a specific magnet assembly. Future studies should incorporate measured or calculated three-dimensional magnetic-field maps, including fringe-field components, to evaluate realistic compact magnet assemblies.

Second, the reported deposited dose values should not be interpreted as complete shielding of all radiation emitted from Cs-137. Photon transport was included in the coupled electron–photon transport calculation; however, the deposited dose reported in this study was restricted to the beta-particle/electron component in the dose-scoring volume. Therefore, the present results represent magnetic deflection shielding performance for the beta-particle/electron component emitted from Cs-137, not the total absorbed dose from all Cs-137 radiation components. In practical radiation-protection applications, conventional passive shielding would still be required for the 661.7 keV gamma-ray component, whereas magnetic deflection shielding may serve as a complementary strategy for reducing exposure to charged beta particles.

Third, the possible reduction of bremsstrahlung production should be interpreted only as a potential advantage of magnetic deflection shielding. Because magnetic deflection can redirect beta particles without direct interception by a solid absorber, absorber-induced bremsstrahlung may be reduced in principle. However, photon fluence and photon dose were not evaluated as outcome quantities in the present study. Therefore, this potential benefit should be quantitatively verified in future work by calculating photon fluence, photon dose, and energy-resolved secondary radiation components.

Finally, the present study evaluated absorbed dose in air as a physical benchmark for magnetic deflection shielding. The results should not be interpreted as direct organ-dose estimates for workers or as a prototype-level performance assessment of a specific shielding device. Future studies should include realistic magnet assemblies, device weight and size constraints, fringe-field distributions, energy-resolved tallies, entrance-plane fluence maps, and application-specific protection targets. Such work will be necessary to translate the present finite-length transport findings into practical compact or mobile active shielding systems.

5. Conclusions

This study investigated magnetic deflection shielding for the beta-particle/electron component emitted from Cs-137 using PHITS Monte Carlo simulations. The results demonstrated that increasing magnetic flux density does not necessarily produce a monotonic improvement in dose reduction when the effective magnetic-field length is short. Instead, the shielding response was governed by the combined effect of magnetic flux density and effective magnetic-field length.

At a source-to-scoring distance of 30 cm, the 1-cm effective magnetic-field length showed a minimum deposited dose rate at 0.8 T, followed by dose rebound at higher magnetic flux densities. This non-monotonic response indicates trajectory over-deflection in a short magnetic-field region. In contrast, the 2- and 3-cm conditions reached practical saturation at approximately 0.4 and 0.3 T, respectively, and further increases in magnetic flux density provided little additional dose-reduction benefit. The additional 15 cm simulation showed a similar length-dependent trend, supporting that the finite-length behavior was not specific to the 30 cm geometry.

These findings indicate that compact magnetic deflection shielding should be designed by optimizing the field–length combination rather than by simply increasing magnetic flux density. In particular, effective magnetic-field lengths of 2–3 cm provided more stable dose-reduction behavior than the 1-cm configuration and may therefore represent a more practical design range for compact or mobile charged-particle shielding devices. A 1-cm configuration may be considered only under severe spatial constraints, and its operating magnetic flux density should be carefully selected to avoid dose rebound caused by over-deflection.

The main scientific contribution of this study is that it reformulates a previously saturated long-field shielding response as a finite-length charged-particle transport problem. By reducing the effective magnetic-field length to 1–3 cm, this study identified finite-length saturation and trajectory over-deflection as key design factors and provided physical guidelines for designing compact magnetic deflection shielding systems for Cs-137 beta particles.

Acknowledgment

This paper was supported by RESEARCH FUND offered from Catholic University of Pusan.

References

[1] S. A. Washburn, S. R. Blattnig, R. C. Singleterry, and S. C. Westover, Life Sci. Space Res. **4**, 22 (2015).
[2] F. Ambroglini, R. Battiston, and W. J. Burger, Front. Oncol. **6**, 97 (2016).
[3] M. Vuolo, M. Giraudo, R. Musenich, V. Calvelli, F. Ambroglini, W. J. Burger, and R. Battiston, Life Sci. Space Res. **8**, 22 (2016).
[4] C.-Y. Huang, B. Yang, W. W. Lam, H. Geng, K. Y. Cheung, and S. K. Yu, Med. Phys. **50**, 3623 (2023).
[5] Y. I. Cho, J. M. Kim, and J. H. Kim, Radiat. Prot. Dosim. **174**, 13 (2017).
[6] W. R. Van Pelt and M. Drzyzga, Health Phys. **92**, S13 (2007).
[7] J. Lelieveld, D. Kunkel, and M. G. Lawrence, Atmos. Chem. Phys. **12**, 4245 (2012).
[8] Y. Cao, L. Zhou, H. Ren, and H. Zou, Int. J. Environ. Res. Public Health **19**, 10183 (2022).
[9] H. Yasuda, Appl. Sci. **11**, 4424 (2021).
[10] N. Petoussi-Henss, W. E. Bolch, K. F. Eckerman, A. Endo, N. Hertel, J. Hunt, M. Pelliccioni, H. Schlattl, and M. Zankl, Ann. ICRP **40**, 1 (2010).
[11] E. T. Sakamoto-Hojo, Mutat. Res. Genet. Toxicol. Environ. Mutagen. **836**, 72 (2018).
[12] J. M. Seo, J. Korean Soc. Radiol. **19**, 847 (2025). https://doi.org/10.7742/jksr.2025.19.7.847
[13] L. Marques, A. Vale, and P. Vaz, Sensors **21**, 1051 (2021).
[14] D. T. Connor, K. Wood, P. G. Martin, S. Goren, D. Megson-Smith, Y. Verbelen, I. Chyzhevskyi, S. Kirieiev, N. T. Smith, T. Richardson, and T. B. Scott, Front. Robot. AI **6**, 149 (2020).
[15] T. Sato, Y. Iwamoto, S. Hashimoto, T. Ogawa, T. Furuta, S.-I. Abe, T. Kai, Y. Matsuya, N. Matsuda, Y. Hirata, T. Sekikawa, L. Yao, P.-E. Tsai, H. N. Ratliff, H. Iwase, Y. Sakaki, K. Sugihara, N. Shigyo, L. Sihver, K. Niita, J. Nucl. Sci. Technol. **61**, 127 (2024).
[16] T. Sato, Y. Iwamoto, S. Hashimoto, T. Ogawa, T. Furuta, S. Abe, T. Kai, P. Tsai, N. Matsuda, H. Iwase, N. Shigyo, L. Sihver, and K. Niita, J. Nucl. Sci. Technol. **55**, 684 (2018).
[17] K. F. Eckerman and A. Endo, Ann. ICRP **38**, 7 (2008).
[18] S. A. Kalospyros, V. Gika, Z. Nikitaki, A. Kalamara, I. Kyriakou, D. Emfietzoglou, M. Kokkoris, and A. G. Georgakilas, Appl. Sci. **11**, 8985 (2021).
[19] H. Hirayama, Y. Namito, A. F. Bielajew, S. J. Wilderman, and W. R. Nelson, SLAC-R-730 and KEK Report 2005-8 (2005).
[20] W. S. Ahn, W. Choi, Y. R. Ka, J. Kwak, I.-H. Jung, S. Ahn, and S. S. Shin, J. Magn. **25**, 409 (2020).